Supporting Information

A self-supported copper/copper oxide heterostructure derived from a copper-MOF for improved electrochemical nitrate reduction

Mengmiao Sun, Guanzheng Wu, Lei Dai, Martin Oschatz, Qing Qin**

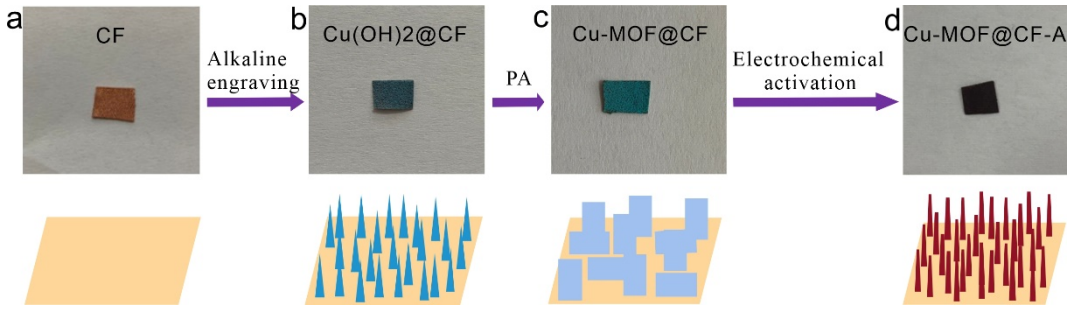

Figure S1. Synthesis of self-supported $Cu(OH)_2$@CF, Cu-MOF@CF and Cu(O)@CF-A materials from pure CF and their corresponding optical images.

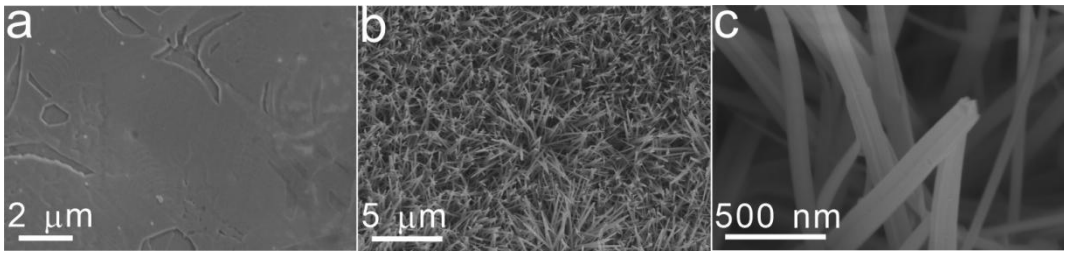

Figure S2. SEM images of (a) CF and (b-c) $Cu(OH)_2$@CF.

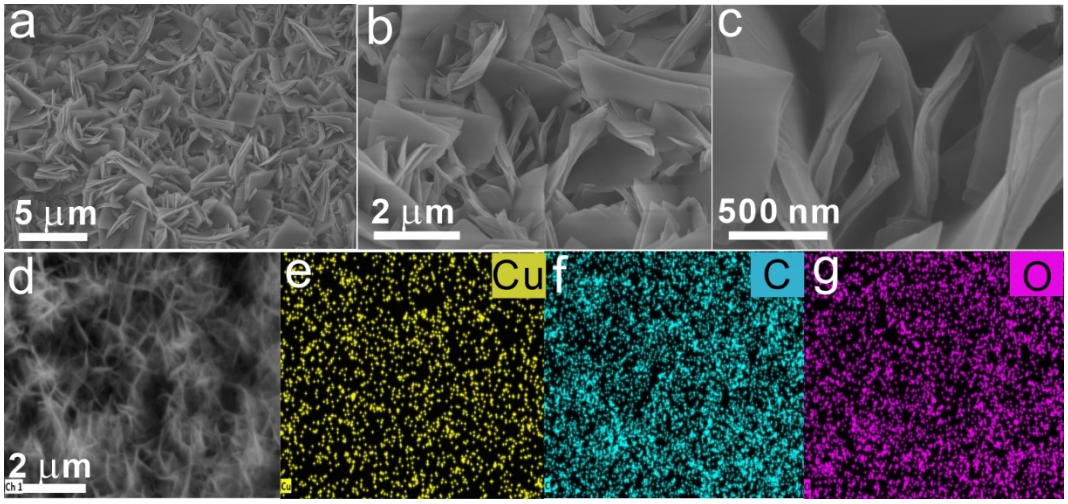

Figure S3. (a-c) SEM images of Cu-MOF@CF; SEM image (d) and the corresponding EDS mapping images of (e) Cu, (f) C and (g) O atoms in Cu-MOF@CF.

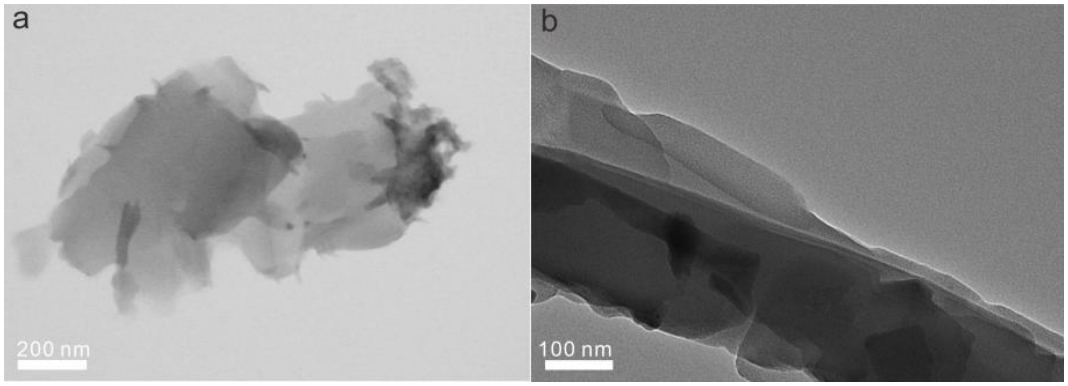

Figure S4. TEM images of Cu-MOF@CF materials.

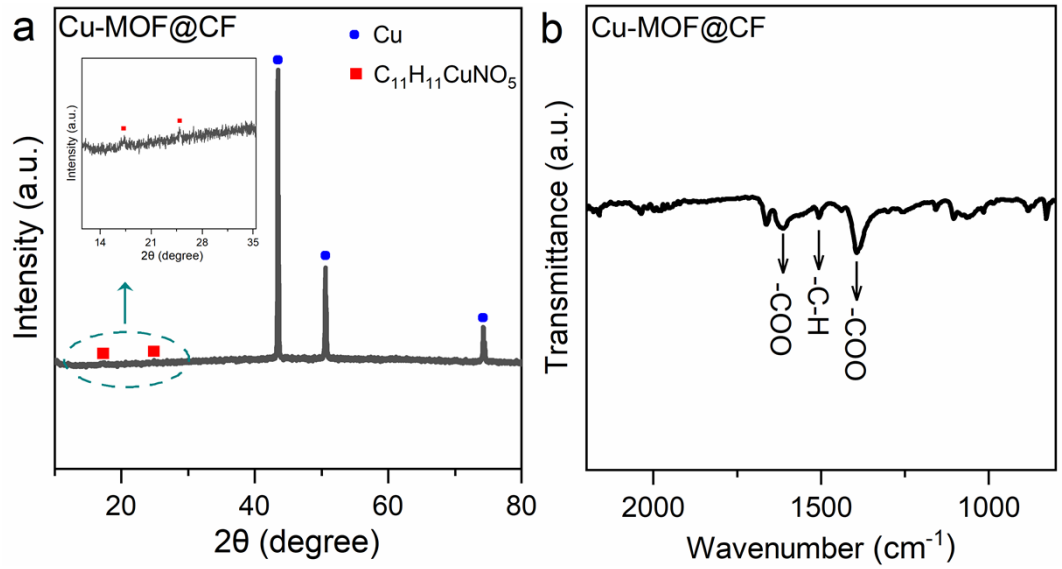

Figure S5. (a) XRD pattern and (b) FT-IR spectrum of Cu-MOF@CF.

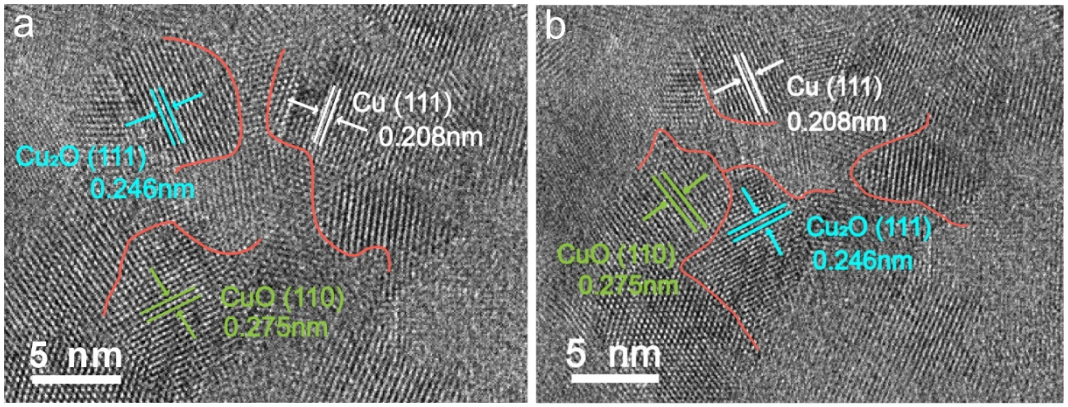

Figure S6. The HRTEM images of Cu(O)@CF-A materials in other selected areas.

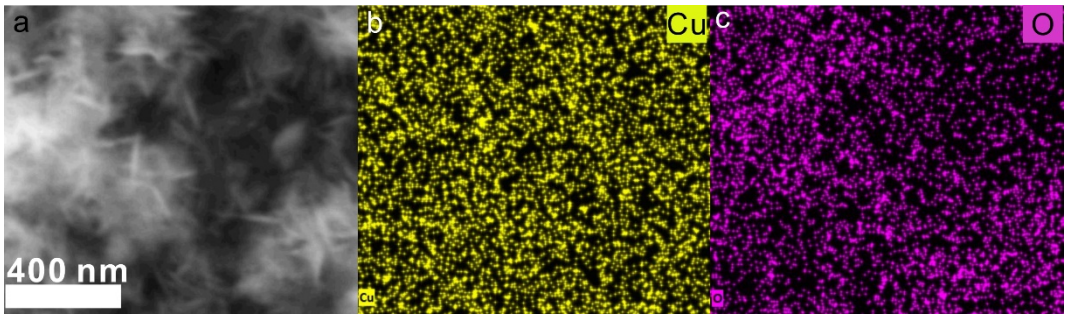

Figure S7. SEM image (a) and the correspongding EDS mapping images of (b) Cu, (c) O atoms in Cu(O)@CF-A.

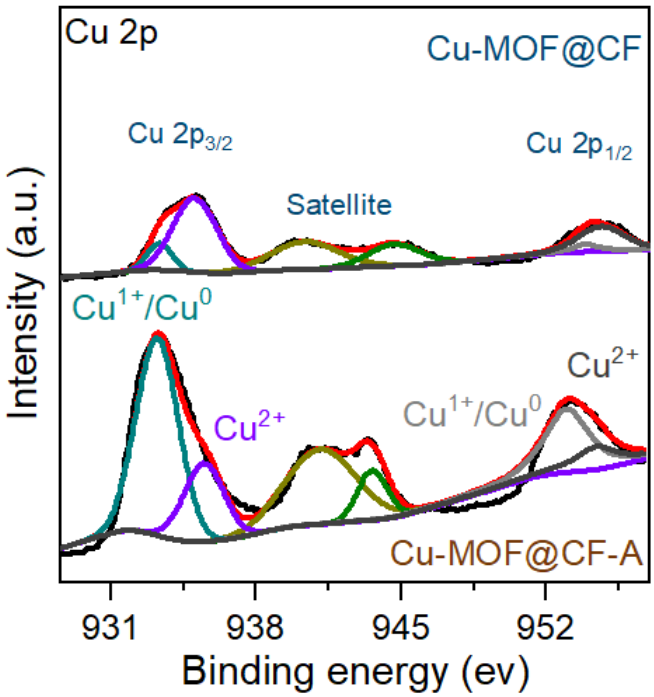

Figure S8. High-resolution XPS spectra of Cu 2p for Cu-MOF@CF and Cu(O)@CF-A.

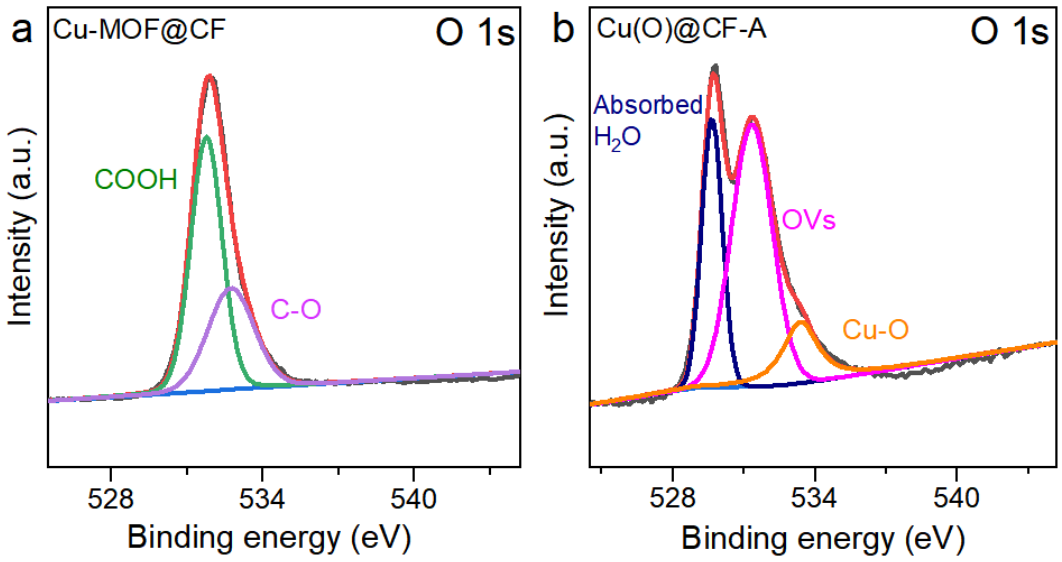

Figure S9. The comparison of high-resolution XPS spectra of O 1s for Cu-MOF@CF and Cu(O)@CF-A.

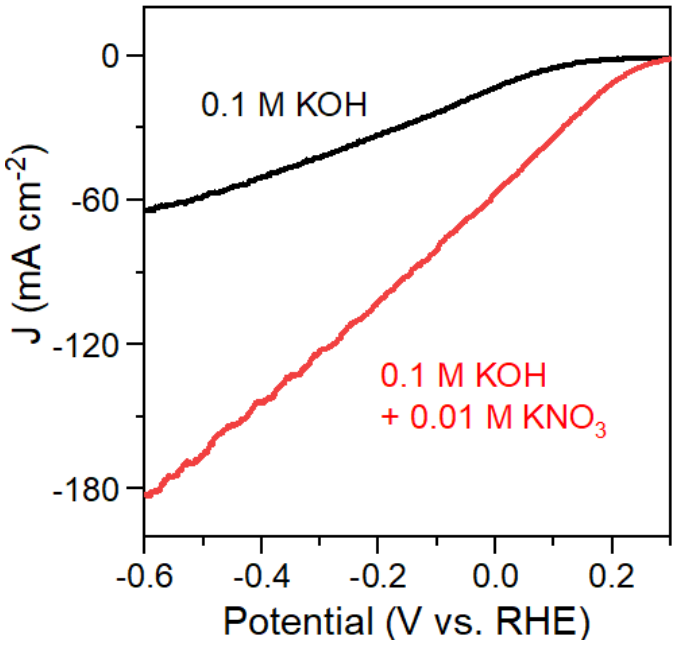

Figure S10. LSV curves of the electrode containing Cu(O)@CF-A with 0.1 M KOH electrolyte solution with and without NO_3^- addition.

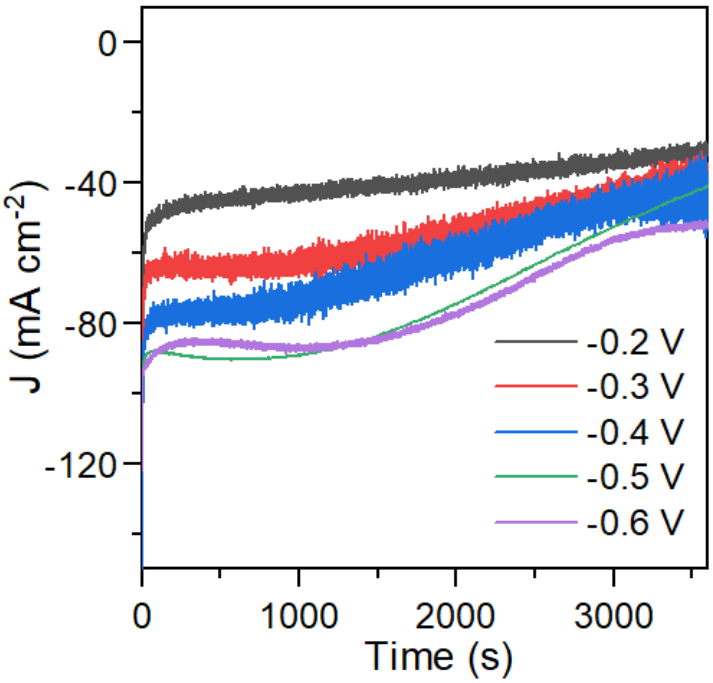

Figure S11. Chronoamperometry results of the electrode containing the Cu(O)@CF-A catalyst at different given potentials (-0.2, -0.3, -0.4, -0.5 and -0.6 V vs. RHE).

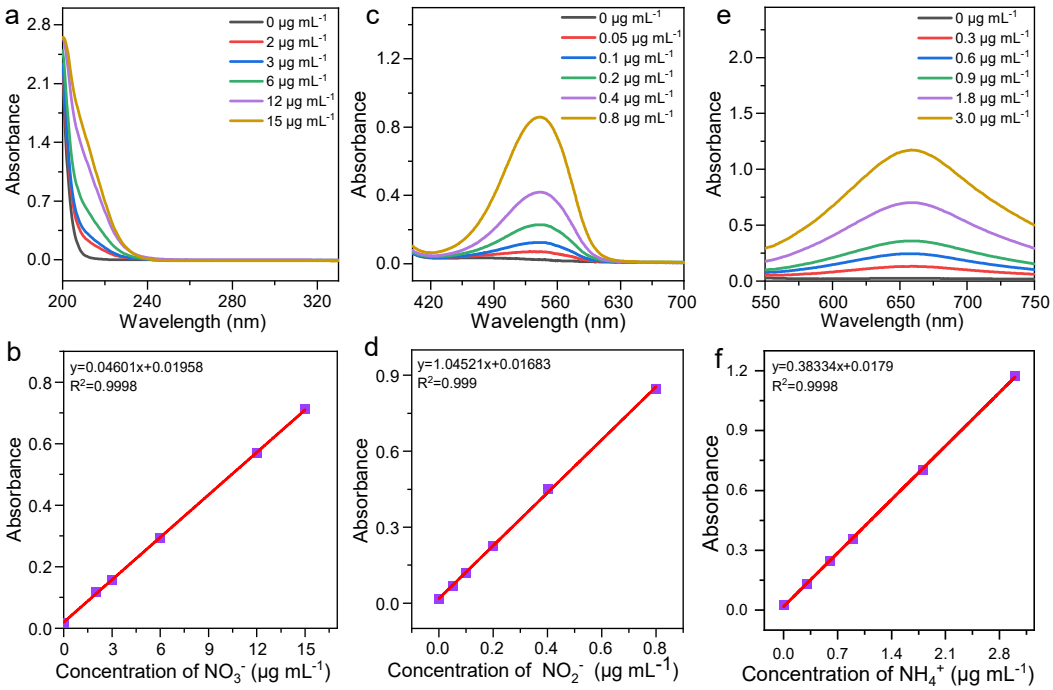

Figure S12. (a) UV-Vis spectroscopy curves of NO_3^- solutions with different known concentration (0, 2, 3, 6, 12, 15 μg mL^{-1}) ($A_{nitrate}=A_{220nm}-2A_{275nm}$). (b) The corresponding linear calibration curve was used to quantify the NO_3^- conversion rate. (c) UV-Vis spectroscopy curves of NO_2^- solutions with different known concentration (0, 0.05, 0.1, 0.2, 0.4, 0.8 μg mL^{-1}) (the absorbance at 540 nm is referred to the concentration of NO_2^-). (d) The corresponding linear calibration curve was used to quantify the NO_2^- yield. (e) UV-Vis spectroscopy curves of NH_4^+ solutions with different known concentration (0, 0.3, 0.6, 0.9, 1.8, 3.0 μg mL^{-1}) (the absorbance at 655 nm is referred to the concentration of NH_4^+). (f) The corresponding linear calibration curve was used to quantify the NH_4^+ yield.

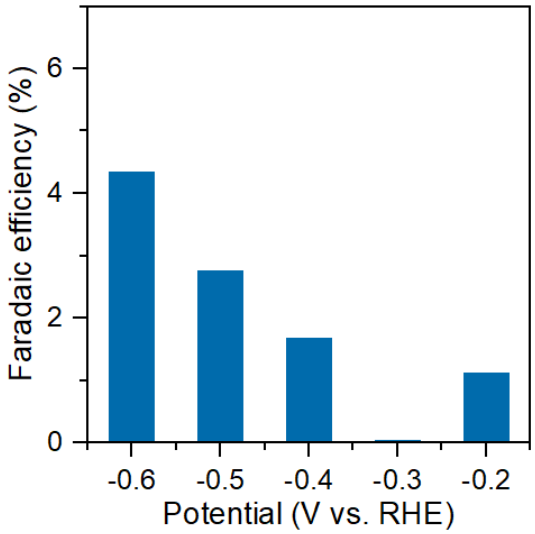

Figure S13. The FE of H_2 at different applied potentials of -0.2 V, -0.3 V, -0.4 V, -0.5 V, -0.6 V.

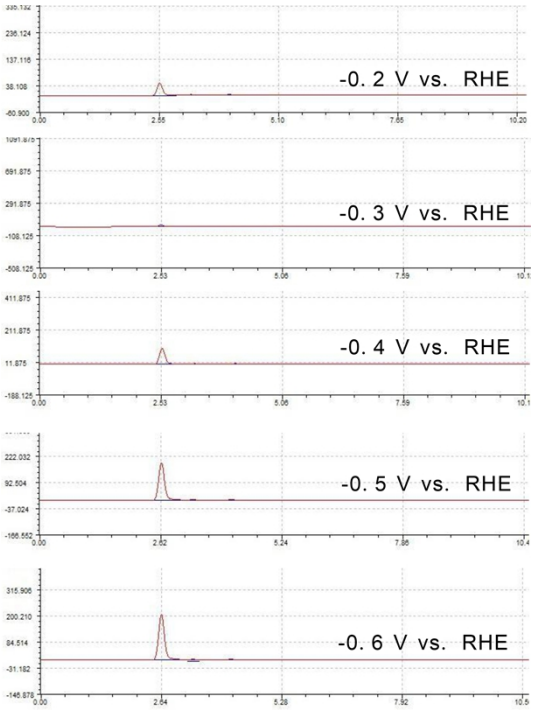

Figure S14. The detection of gaseous products in NITRR by GC at different applied potentials of -0.2 V, -0.3 V, -0.4 V, -0.5 V, -0.6 V.

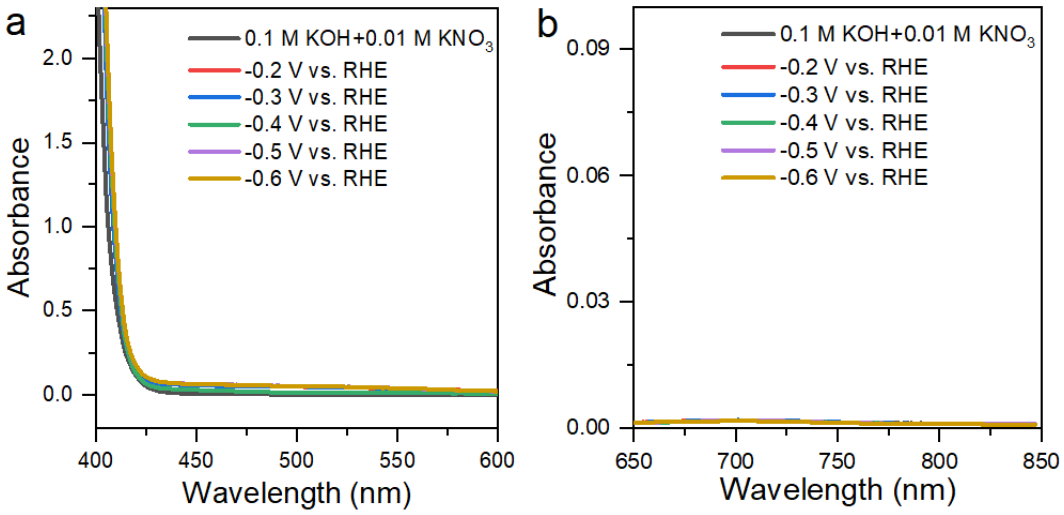

Figure S15. UV-Vis spectroscopy curves for (a) N_2H_4 and (b) NH_2OH detection under the potential of -0.2 V, -0.3 V, -0.4 V, -0.5 V, -0.6 V.

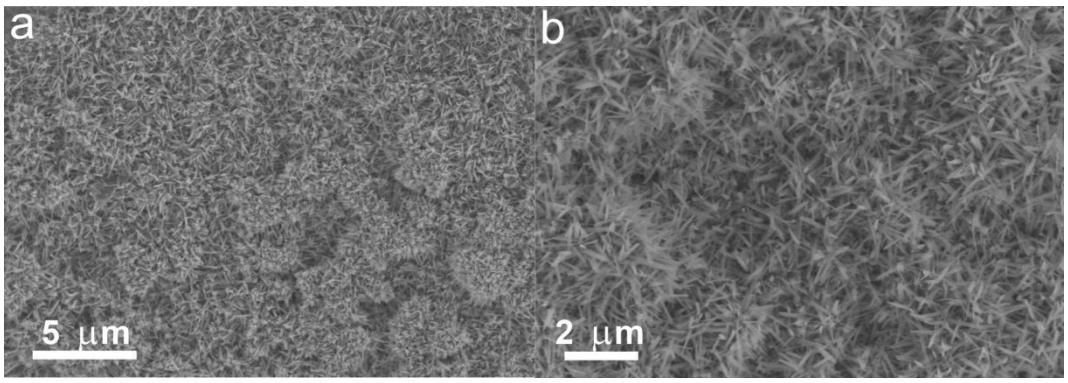

Figure S16. SEM images of the Cu(O)@CF-A catalyst after the cycle test.

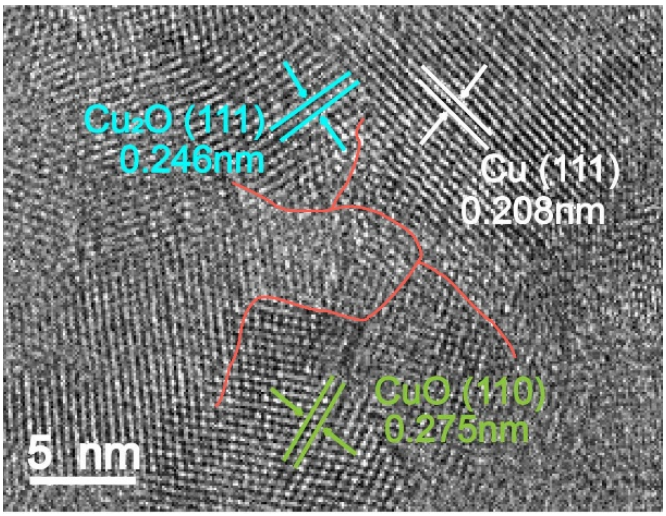

Figure S17. The HRTEM images of Cu(O)@CF-A after the cycle test.

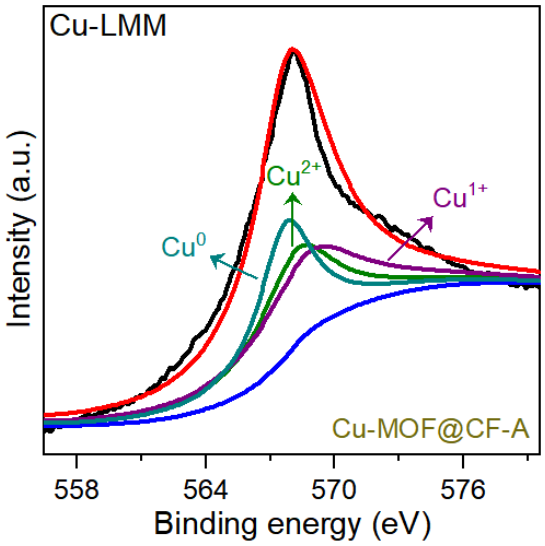

Figure S18. The XPS results of Cu(O)@CF-A after the cycle test.

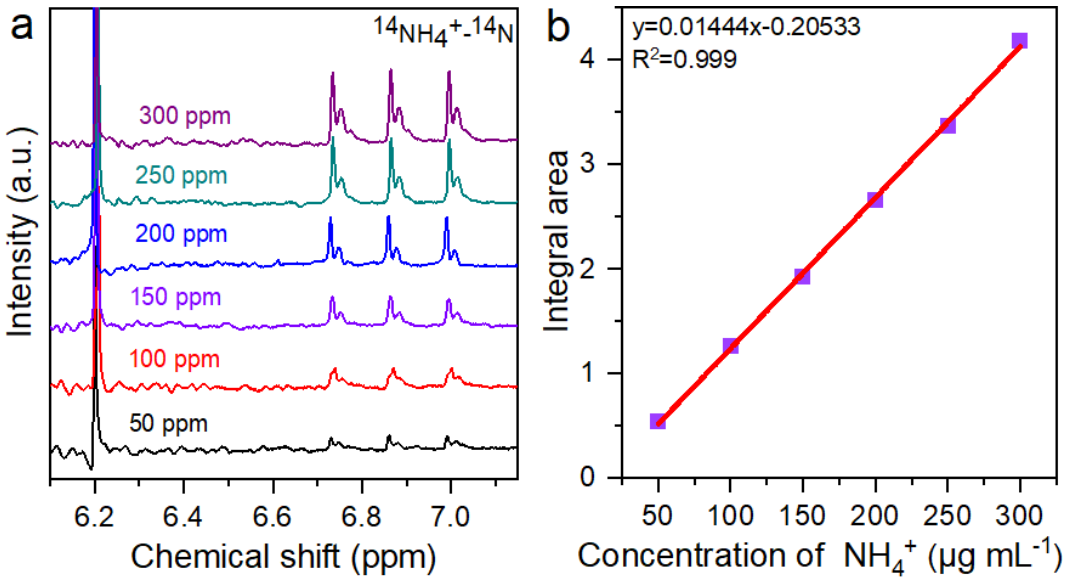

Figure S19. (a) ^{1}H-NMR curves of NH_4^+ solutions with different known concentration (50, 100, 150, 200, 250 and 300 ppm). (b) The corresponding linear calibration curve through ^{1}H-NMR measurement was used to quantify the NH_4^+ yield.

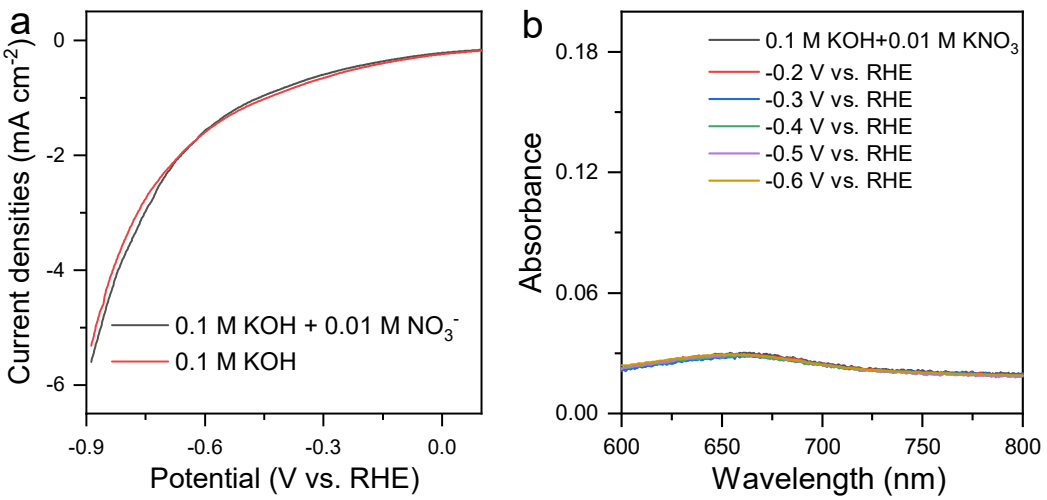

Figure S20. The performance of carbon paper in nitrate reduction: (a) LSV curves with and without the addition of nitrate. (b) UV-Vis spectroscopy curves for NH_3 detection after the electrocatalysis under the potential of -0.2 V, -0.3 V, -0.4 V, -0.5 V, -0.6 V.

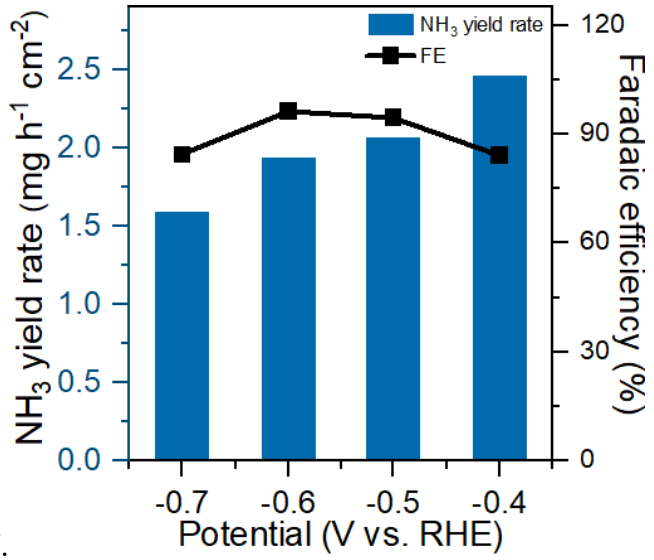

Figure S21. Cu(O)@CF-A electrode: The FE and yield rate toward NH_3 in the 0.1 M Na_2SO_4 containing 0.01 M NO_3^- (-0.4, -0.5, -0.6 and -0.7 V vs. RHE). -

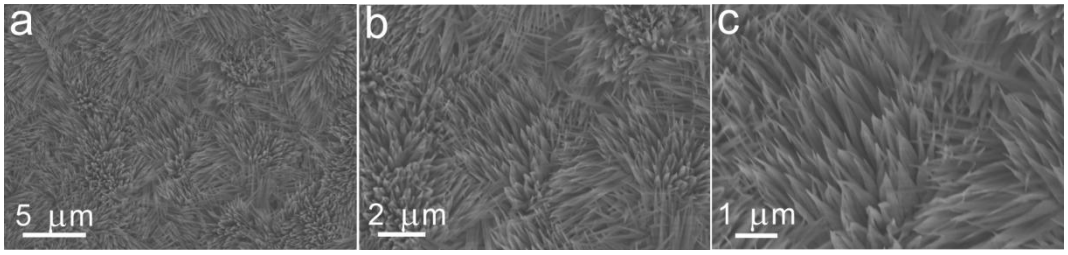

Figure S22. SEM images of as-synthesized NiFe LDH used as the anode catalysts.

Figure S23. NITRR driven by the solar cell under the irradiation of natural sunlight. The optical image of the (a) electrochemical cell, (b) anodic part with obvious gas bubbles on the NiFe LDH electrode and (c) cathodic part with no gas bubble on the Cu(O)@CF-A electrode.

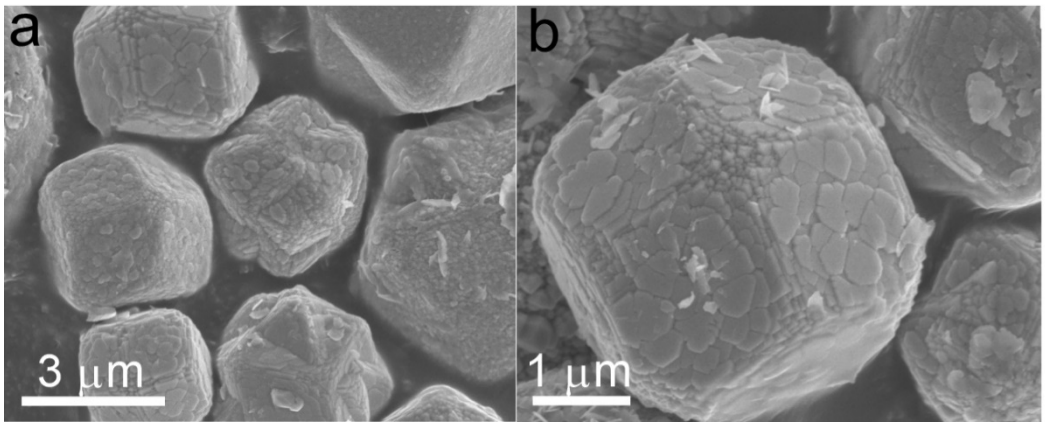

Figure S24. (a-b) SEM images of Cu-MOF particles by using $CuCl_2$ as precursors, instead of $Cu(OH)_2$@CF.

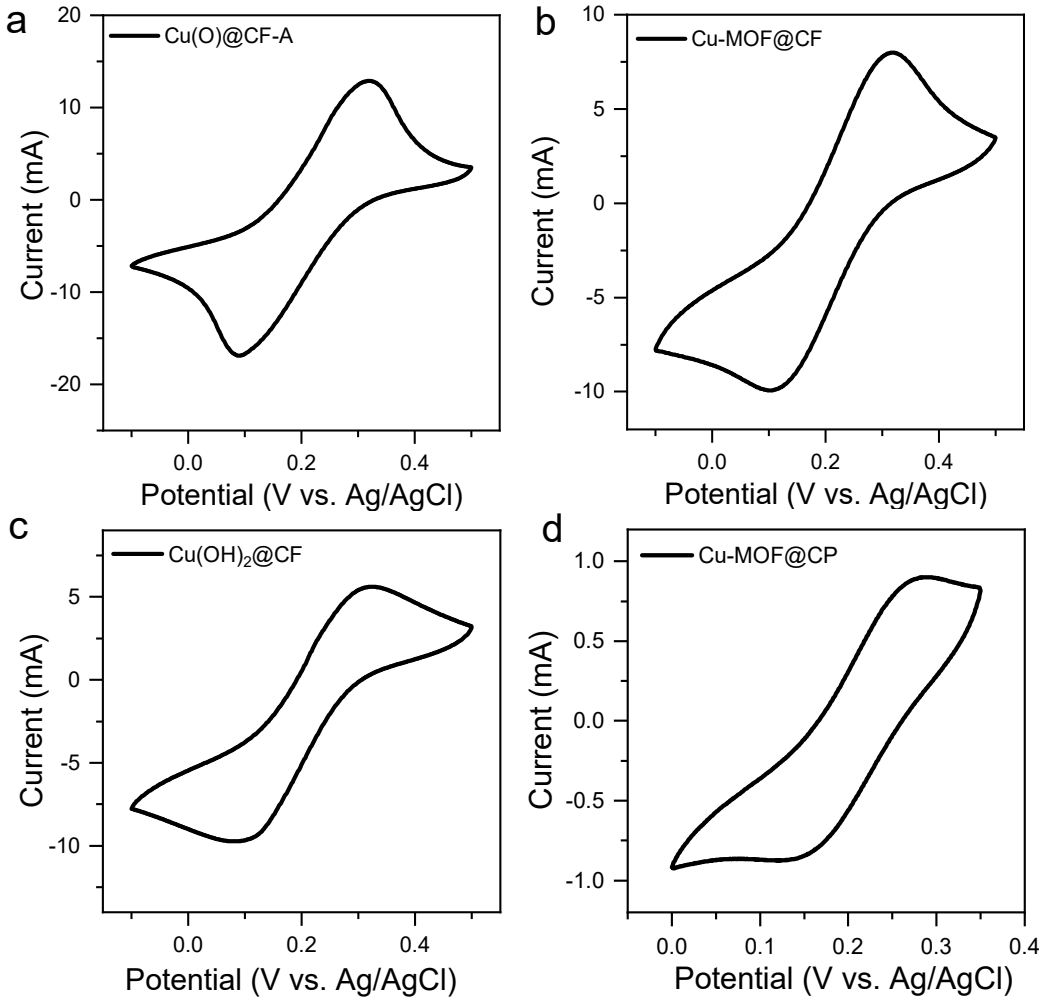

Figure S25. CV curves of ECSA for various electrodes in 0.1 M KCl solution containing 50 mM $K_3Fe(CN)_6$. The scan rate is 10 mV s^{-1}. The ECSA was determined by the Randles-Sevcik equation, calculated and summarized in Table S2.

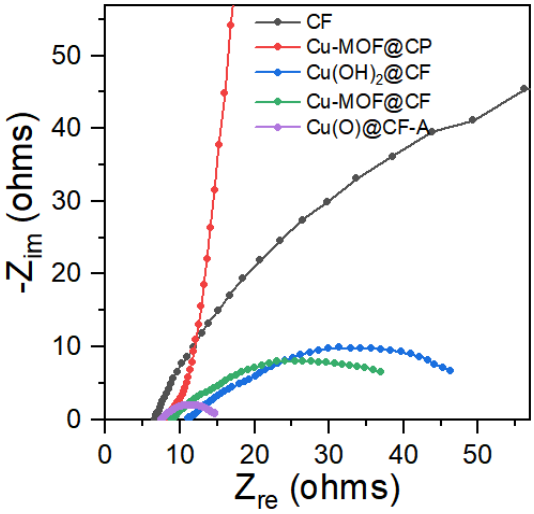

Figure S26. EIS measurements of Cu(O)@CF-A, Cu-MOF@CF, $Cu(OH)_2$@CF, Cu-MOF@CP and pure CF.

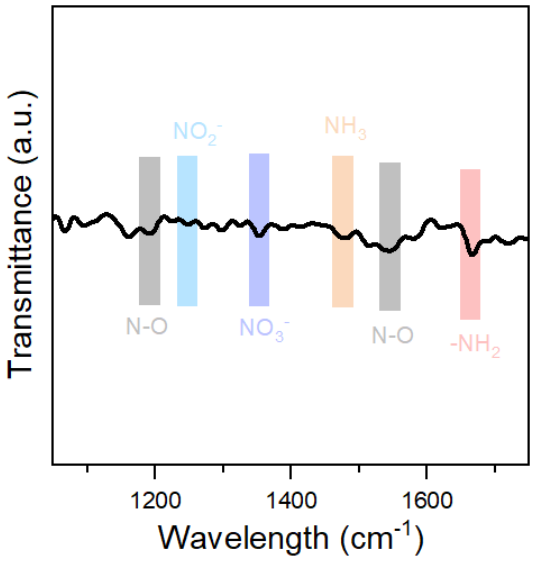

Figure S27. In situ FT-IR spectra of Cu(O)@CF-A electrode during NITRR at the potential of -0.3 V vs. RHE.

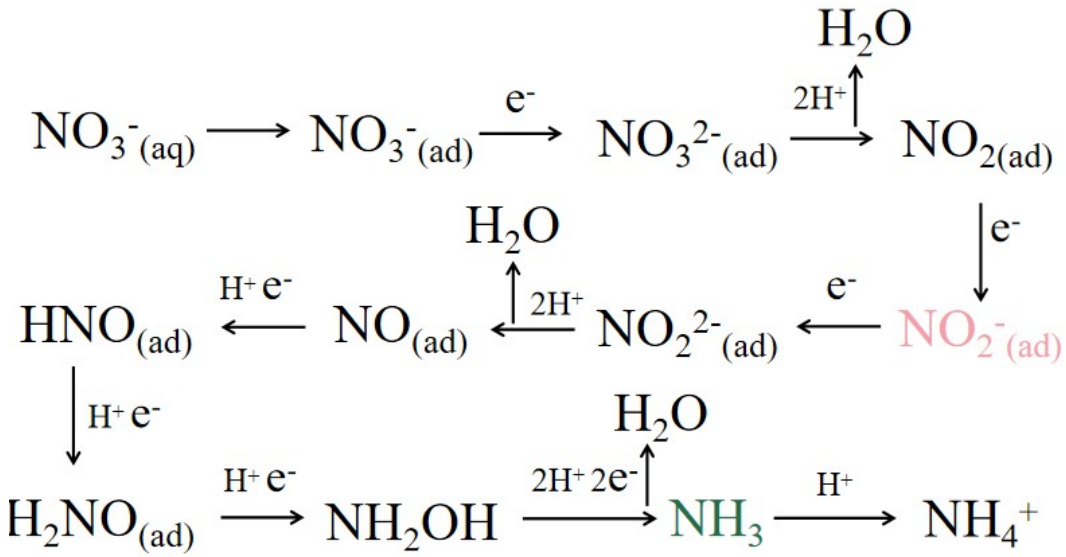

Figure S28. The possible pathways of NITRR for Cu(O)@CF-A electrode.

Table S1. The comparison of the FE, NH_3 yield rate, and NH_3 selectivity of different Cu-based electrocatalysts in recently published results.

Electrocatalyst	Electrolyte	FE	NH_3 yield rate	NH_3 Selectivity	Ref
Cu(O))@ CF-A	**0.01 M KNO_3 + 0.01 M KOH**	**99.5 %**	**5.9 mg h^{-1} cm^{-2}**	**97.1 %**	**This work**
Cu-Pt (180s)	0.01 M $NaNO_3$ + 0.1 M Na_2SO_4		194.4 mg L^{-1} g_{cat}^{-1}	84 %	1
PA-RhCu cNCs	0.05 M KNO_3 + 0.1 M $HClO_4$	93.7 %	2.40 mg h^{-1} mg_{cat}^{-1}		2
CuO_x	50 ppm KNO_3 + 0.1 M KOH	74.18 %	449.41 μg h^{-1} mg_{cat}^{-1}		3
Cu_2O (100)	50 ppm KNO_3 + 0.1 M KOH	82.3 %	743 μg h^{-1} mg_{cat}^{-1}		4

Cu_2O	0.05 M KNO_3 + 0.5 M Na_2SO_4	98.28 %		96.6 %	5
Cu/Cu-Mn_3O_4 NSAs/CF	200 mg L^{-1} KNO_3 + 0.5 M K_2SO_4	92.4 %	0.21 mmol h^{-1} cm^{-2}	87.6 %	6
Cu/Cu_2O NWAs	200 ppm $NaNO_3$ + 0.5 M $NaSO_4$	95.8 %	0.2449 mmol h^{-1} cm^{-2}	81.2 %	7
Cu (111)	0.01 M KNO_3 + 0.1 M KOH	81.1 %	2.16 mg mg_{cat}^{-1} h^{-1}		8
Cu-N-C	1 M KNO_3 + 1 M KOH	95.5 %	13.8 mol g_{cat}^{-1} h^{-1}		9
Pd-Cu_2O CEO	50 ppm KNO_3 + 0.5 M K_2SO_4	96.56 %	925.11 μg h^{-1} mg_{cat}^{-1}	95.31 %	10

Table S2. The electrochemical surface area of Cu(O)@CF-A, Cu-MOF@CF, $Cu(OH)_2$@CF and Cu-MOF@CP estimated by probing the redox reaction of ferricyanide/ferrocyanide using cyclic voltammetry (CV).

Sample	Cu(O)@CF-A	Cu-MOF@CF	Cu(OH)2@CF	Cu-MOF@CP
ECSA/cm^2	3.42	2.102	1.478	0.242

Reference

1 Cerrón-Calle, G. A., Fajardo, A. S., Sánchez-Sánchez, C. M. et al. Highly reactive Cu-Pt bimetallic 3D-electrocatalyst for selective nitrate reduction to ammonia, *Appl. Catal. B-Environ.*, **2022**, *302*, 120844.

2 Ge, Z. X., Wang, T. J., Ding, Y. et al. Interfacial Engineering Enhances the Electroactivity of Frame-Like Concave RhCu Bimetallic Nanocubes for Nitrate Reduction, *Adv. Energy Mater.*, **2022**, *12*, 2103916.

3 Geng, J., Ji, S., Xu, H. et al. Electrochemical reduction of nitrate to ammonia in a fluidized electrocatalysis system with oxygen vacancy-rich CuO_x nanoparticles, *Inorg. Chem. Front.*, **2021**, *8*, 5209-5213.

4 Qin, J., Chen, L., Wu, K. et al. Electrochemical Synthesis of Ammonium from Nitrates via Surface Engineering in Cu_2O (100) Facets, *ACS Appl. Energy Mater.*, **2022**, *5*, 71-76.

5 Wang, C., Ye, F., Shen, J. et al. In Situ Loading of Cu_2O Active Sites on Island-like Copper for Efficient Electrochemical Reduction of Nitrate to Ammonia, *ACS Appl. Mater. Inter.*, **2022**, *14*, 6680-6688.

6 Wang, H., Mao, Q., Ren, T. et al. Synergism of Interfaces and Defects: Cu/Oxygen Vacancy-Rich Cu-Mn_3O_4 Heterostructured Ultrathin Nanosheet Arrays for Selective Nitrate Electroreduction to Ammonia, *ACS Appl. Mater. Inter.*, **2021**, *13*, 44733-44741.

7 Wang, Y., Zhou, W., Jia, R. et al. Unveiling the activity origin of a copper-based electrocatalyst for selective nitrate reduction to ammonia, *Angew. Chem. Int. Ed.*, **2020**, *59*, 5350-5354.

8 Wu, K., Sun, C., Wang, Z. et al. Surface Reconstruction on Uniform Cu Nanodisks Boosted Electrochemical Nitrate Reduction to Ammonia, *ACS Mater. Lett.*, **2022**, *4*, 650-656.

9 Xu, M., Xie, Q., Duan, D. et al., Atomically Dispersed Cu Sites on Dual-Mesoporous N-Doped Carbon for Efficient Ammonia Electrosynthesis from Nitrate, *ChemSusChem*, **2022**, doi.org/10.1002/cssc.202200231.

10 Xu, Y., Ren, K., Ren, T. et al. Ultralow-Content Pd In-Situ Incorporation Mediated Hierarchical Defects in Corner-Etched Cu_2O Octahedra for Enhanced Electrocatalytic Nitrate Reduction to Ammonia, *Appl. Catal. B-Environ.*, **2022**, *306*, 121094.